Photonic band effects in a two-dimensional array of dielectric spheres in the millimeter-wave region

K. Ohtaka, Y. Suda, S. Nagano, and T. Ueta
Department of Applied Physics, Faculty of Engineering, Chiba University, Chiba 263-8522, Japan

A. Imada and T. Koda
Department of Mathematical and Physical Sciences, Faculty of Science, Japan Women's University, Tokyo 112-8681, Japan

J. S. Bae and K. Mizuno
Research Institute of Electrical Communication, Tohoku University, Sendai 980-8577, Japan

S. Yano and Y. Segawa
Photodynamics Research Center, The Institute of Physical and Chemical Research (RIKEN), Sendai 980-0868, Japan
(Received 6 April 1999)

The transmission and phase-shift spectra for millimeter electromagnetic waves are obtained for a two-dimensional (2D) square lattice array made of Si_3N_4 spheres of diameter $\simeq 3.2$ mm. The results are compared with the theoretical 2D photonic-band structures that take account of the lifetime effect due to the radiative energy decay. It is found that the incidence-angle dependence of the observed transmission spectra is in excellent agreement with the calculated in-plane dispersion curves of the photonic bands and that the frequency dependence of the phase shift agrees well with the calculated lifetime-broadened density of states. The radiative lifetimes of the photonic bands are estimated to be about ten times longer than those of whispering gallery modes of an isolated sphere, though the magnitudes depend rather strongly on the wave vector and band index.

I. INTRODUCTION

The band structures of photons in photonic crystals have attracted growing interest both theoretically and technologically.[1–3] Although experimental endeavors have so far been concentrated on several urgent technological objectives,[4–6] such as the realization of all-directional stop bands and the introduction of a gap mode in a stop band,[7,8] the future role of photonic crystals is not limited solely to the field of technology. They will provide us with new topics in basic science; the photon localization in an amorphous photonic crystal[9] and the photonic property worthy of the name ''heavy photon'' are two such examples already familiar to us.[10]

Among a number of types of photonic crystals, periodic arrays of dielectric spheres are a prototype of photonic crystals.[11,12] The photonic band effect in such systems has been under active study both theoretically[13–16] and experimentally.[17–21] They are a target of the recent extensive studies of the basic properties of photonic crystals, such as orthonormality of eigenmode functions,[10,22] group-theoretical properties,[23] and energy flow and birefringence.[24] One important advantage of photonic crystals of this category is that their physics is understood by using the ample knowledge of electrons of ordinary solid-state systems, with their dielectric spheres regarded as ''optical'' atoms. In fact, with such an analogy in mind, the concept of photonic bands was introduced and formulated by Ohtaka in the late 1970's.[25] Peculiar resonant enhancement in optical processes, the confinement effect of electromagnetic (EM) waves in the terms of today, was already recognized in the earlier 1980's.[26–29] As this example shows, the optical properties of lattice of spheres are, with minor quantitative correction, mostly common to more sophisticated types of artificial photonic crystal. In this sense, systems of arrayed spheres are of fundamental importance to understand photonic crystals.

This paper deals with the photonic band effects in a monolayer square lattice of dielectric spheres. Since the experiments and applications of photonic crystals are usually made for a slab photonic crystal with thickness of a few or several periodicities, they are governed in many ways by the two-dimensional (2D), rather than 3D, properties of photonic bands. The study of the properties of a monolayer system of spheres, such as the density of states of photonic bands and their radiative lifetime, thus provides us with good insight into actual photonic crystals of finite thickness. In a preceding companion paper,[30] theoretical aspects of the near-field properties of a monolayer of spheres were discussed. The present paper treats the far-field properties of the same system. We present the experimental results and their theoretical analysis.

The first aim of the present paper is to examine how the theory and experiment agree with respect to the dispersion relation of photonic bands of the monolayer system. Due to the lack of translational invariance, the treatment of the normal modes of a slab system is nontrivial. We will propose several theoretical methods to deal with the dispersion relation and show that the experimental results agree very well with the exact calculation. Another feature of a slab photonic crystal is a finite lifetime of its normal modes due to the energy leakage out of the system through far-field channels.

This feature is analogous to the radiative lifetime of whispering gallery (WG) modes in a spherical microcavity.[31] The second aim of the present study is to obtain information, both experimentally and theoretically, on how lifetimes change when microparticles are assembled together to form a monolayer periodic system.

In the experimental papers cited above and other earlier publications,[3] we find a number of pioneering experiments for the dispersion relations of photonic crystal of spherical particles. However, those optical data are all rather poor for the comparison with the exact theoretical calculation. Our experiment will be carried out using a monolayer lattice of Si_3N_4 beads of millimeter size to obtain transmission and phase-shift spectra of EM waves of mm range. Because of the scalability of the wavelength of EM fields, the conclusions drawn for the millimeter range should apply to the photonic band effect in the visible light range. As for the experimental confirmation and analysis of other types of photonic crystals, we refer the readers to the work of Robertson *et al.*[32] and a very recent work by Kao *et al.*[33]

This paper is arranged as follows. In Sec. II the experimental setup used to obtain the millimeter wave spectra is presented. The observed transmission and phase-shift spectra are compared with calculations in Sec. III. Several characteristic quantities that are useful for studies on lifetime-broadened modes are presented in Sec. IV, and their frequency dependences are analyzed in Sec. V for our lattice of Si_3N_4 spheres. In Sec. VI, we present the theoretical dispersion curves of damped photonic bands together with the discussion on their lifetime. Section VII is a summary of our study. Supplementary description of the phase shifts in light scattering in a monolayer lattice is given in the Appendix.

II. EXPERIMENTAL PROCEDURES

The building blocks for the monolayer photonic crystal we used are spherical balls of Si_3N_4 (made by Toshiba Tungaloy Co., TD.) with diameter $d=1/8$ inch. The Si_3N_4 ball has a fairly high dielectric constant $\varepsilon=8.67(n=2.95)$ in the millimeter wavelength region investigated. We have checked that the loss for the electric field is 4.5×10^{-3}/mm in the frequency range $\omega/2\pi=40$–60 GHz examined in the present study. These Si_3N_4 balls are used for high-precision ball bearings and are therefore guaranteed to possess a highly perfect spherical shape and quite uniform size. Nonuniformity of diameter is less than 0.0005 inches. A monolayer square lattice of lattice constant $a_L=d$ was made by using 25×25 spheres, as shown in Fig. 1. For the calculations, the monolayer plane of the spheres was made in the xy plane, with the x and y axes along the two sides of a square unit cell.

The intensity and phase-shift spectra were measured simultaneously for the transmitted wave, by using a network analyzer (WILTRON 360B) as a function of the millimeter wave frequency for various angles of incidence. The experimental configuration of the measurement is shown in Fig. 2. Two horn antennas were used to produce a probe EM wave and to detect the transmission. We used two lenses ($f=300$ mm) to make a plane-wave incident EM wave and to focus its transmitted component. The plane of incidence of the EM wave was kept in the xz plane by keeping the rotation axis of the layer fixed in the y direction in the oblique incidence. An incident wave then excites a 2D photonic band mode whose 2D $\boldsymbol{k}$ vector is on the symmetry axis Γ-X of the 2D Brillouin zone. Measurements were made for both S- and P-polarized EM waves. The incident $S(P)$ wave produces only the S- (P) polarized transmitted or reflected wave because of the mirror symmetry in the xz plane of the entire geometry.

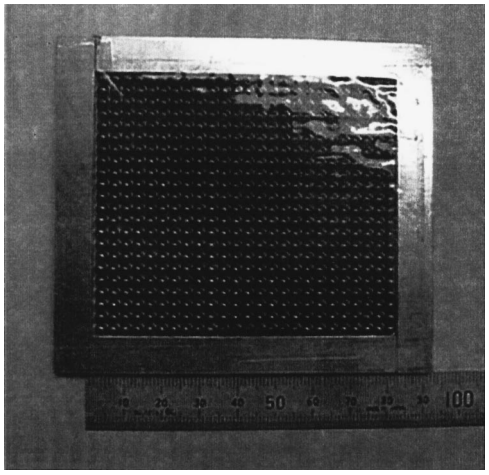

FIG. 1. Photograph of the monolayer square lattice of Si_3N_4 spheres used in the measurement.

When the frequency $\omega/2\pi$ of the incident wave is increased with a fixed angle of incidence θ, first-order Bragg diffraction occurs at the critical frequency $\omega_c/2\pi$ given by $\omega_c/2\pi=c/\{a_L(1+\sin\theta)\}$. This gives, for instance, $\omega_c/2\pi$

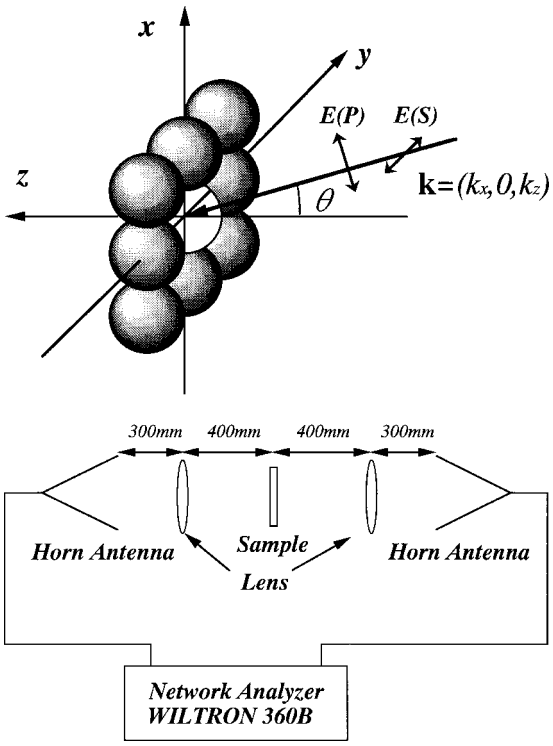

FIG. 2. Experimental configuration to obtain the transmittance and phase-shift spectra. $E(S)$ and $E(P)$ represents the amplitudes of the incident EM wave for S and P polarizations, respectively. The incident plane is the xz plane and θ is the angle of incidence.

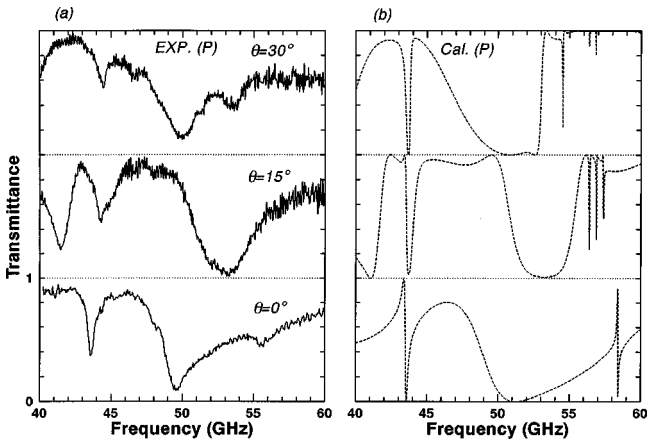

FIG. 3. Transmittance of P wave for a square lattice of Si_3N_4 spheres. (a) Shows the experimental results for the incidence angles of 0°,15°, and 30°. (b) Shows the calculated results for $|T_0|^2$, introduced after Eq. (4.9). The horizontal axis represents frequency in the range 40 GHz$<\omega/2\pi<$60 GHz.

$=96.7$ GHz for $\theta=0°$ and 64.5 GHz for $\theta=30°$. In the frequency range of $\omega/2\pi=40$–60 GHz and the angle range of $\theta=0°$–45°, scanned in the present study, first-order Bragg diffraction does not occur except in the frequency range very near $\omega_c/2\pi=60$ GHz of oblique incidence with θ above 35°. Therefore, we did not examine the diffraction effect in this study.

III. EXPERIMENTAL RESULTS AND COMPARISON WITH CALCULATIONS

A. Transmission spectra

Typical experimental results for P- and S-polarized transmission spectra are shown as functions of frequency $\omega/2\pi$ in Figs. 3(a) and 4(a), respectively, for three incidence angles, $\theta=0°$,15°, and 30°. When we increase θ from zero, a remarkable difference between P and S polarizations appears. Let us first examine the case of P. We note that the dips at $\theta=0°$ change both in position and shape. At $\theta=15°$, different structures appear at frequencies near 42 and 44 GHz. The structure of 42 GHz shifts with increases in θ and goes out of

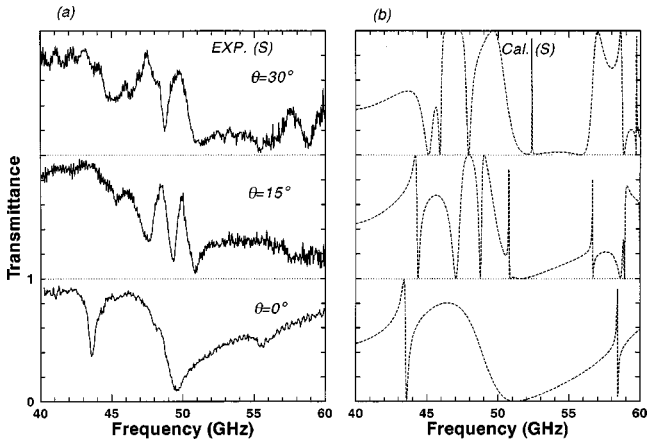

FIG. 4. Transmittance of S wave. (a) and (b) show, respectively, the experimental and theoretical results for the three incidence angles.

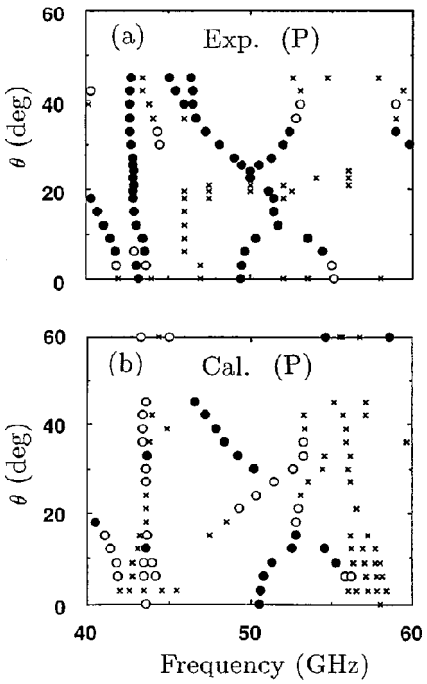

FIG. 5. Positions of dips in transmittance of P wave in the experimental results (a) and the theoretical results (b). The horizontal axis is $\omega/2\pi$, and the vertical axis is the incidence angle θ. The step of θ is 3°. The dips are divided roughly into three classes and given different marks according to their depths (see text).

the examined range at $\theta=30°$. In contrast, the structure at 44 GHz is not so sensitive to θ and remains at rest at $\theta=30°$.

In the higher-frequency region ($\omega/2\pi\geqslant 50$ GHz), the spectral features are much more complicated. Due to the overlapping of considerable background noises, it is no longer possible to identify fine structures. Also, the θ dependence of the spectra in this region is much greater than that in the case of a lower-frequency region. At $\theta=15°$, a broad hump appears above the main dip. Presumably, several small fine structures are superposed upon it. As θ increases, this hump becomes broader together with the shift in the position of the main dip. At $\theta=30°$, a single broad peak is observed at $\omega/2\pi\simeq 50$ GHz. On both sides of this peak, there are a pair of dips at $\omega/2\pi\simeq 47$ and 53 GHz.

In the spectrum of the S polarization shown in Fig. 4(a), the large dip at 49 GHz at $\theta=0°$ is split into three narrow dips at $\theta=15°$. At $\theta=30°$, one of these three dips is found at a low frequency, another at a slightly higher frequency, and the third (located at the highest frequency) remains at rest at $\omega/2\pi\simeq 51$ GHz. In the frequency range above 50 GHz, where fine structures are hard to resolve at $\theta=0°$, a small dip is seen to develop at $\theta=15°$ around $\omega/2\pi\simeq 57$ GHz, and at $\theta=30°$, two small dips are clearly seen near 55 and 58 GHz. Comparing the spectra for $\theta=0°$,15°, and 30° in Figs. 3(a) and 4(a), we can conclude that the fine structures in the P and S spectra are quite independent of each other, although they are identical at $\theta=0°$. In Figs. 5 and 6, we summarize the observed angle dependences of the *dips* in transmittance, using solid circles, open circles, and crosses, which stand for the deep, intermediate, and shallow dips, respectively. The reason for plotting the dip positions will be given in Sec. V. A comparison of Fig. 5(a) and Fig. 6(a)

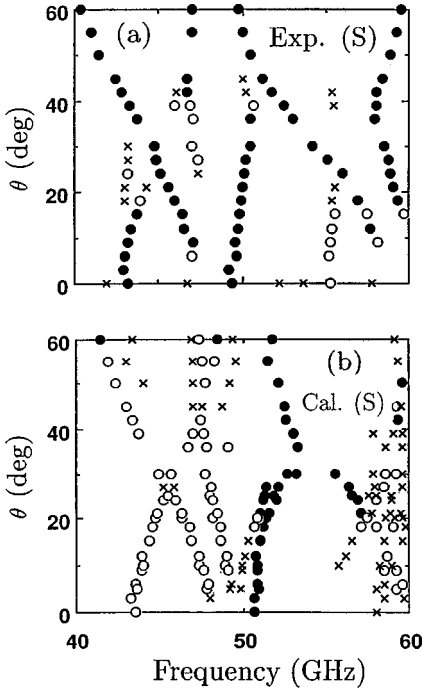

FIG. 6. Positions of dips in transmittance of *S* wave in the experimental results (a) and the theoretical results (b). See the caption of Fig. 5.

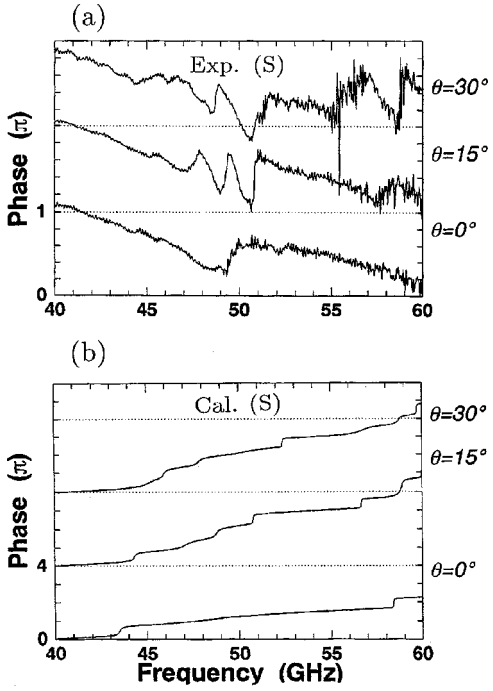

FIG. 7. Phase of the transmitted amplitude for *S* wave. The observed results (a) and theoretical results (b) for incidence angles of 0°,15°, and 30° are given. The vertical axis shows the phase in units π.

shows that the similarity between *P* and *S* spectra at $\theta=0°$ is quickly lost as θ increases. From these figures, we can obtain the experimental ω-k_x relations for the respective fine structures (dip positions) using the relation

$$k_x=\frac{\omega}{c}\sin\theta. \tag{3.1}$$

According to Figs. 5 and 6, the *P*- and *S*-active dips degenerate at $k_x=0$, but they split into each component at off-normal incidence ($k_x\neq 0$).

Now we compare these experimental results with theoretical calculations. Calculations were done for $a_L=d=3.2$ mm and $\varepsilon=8.67$. The calculated transmission spectra are shown in Figs. 3(b) and 4(b) for the *P*- and *S*-polarized waves, respectively. The theoretical formalisms used in the calculation will be given in Sec. IV. In the high-frequency region ($\omega/2\pi>55$ GHz), several theoretically predicted fine structures are yet to be resolved experimentally. In spite of these discrepancies, it is clear that most of the experimental features, including spectral shapes and angle dependences, are reproduced quite well by the theoretical results for both polarizations. For instance, the spectra shown in Figs. 5(b) and 6(b), which display the calculated dip positions as a function of θ, confirm the validity of the present theoretical analysis. The agreement is remarkable if we consider the fact that we used only two material parameters of the diameter $d=a_L$ and the dielectric constant ε.

B. Phase-shift spectra

The observed phase shift of transmitted amplitude relative to that of the incident wave is shown in Fig. 7 for the *S*-polarized wave, in comparison with the theoretical result. Since the discussion for the *P* polarization is similar, we will confine ourselves to the *S* phase shift. In the experimental results, the phase decreases with increase of the frequency due to the reference delay of the network analyzer itself. And also the phase-shift signal has a step at each 2π shift from $-\pi$ to $+\pi$. These two factors make the analysis of the experimental data somewhat controversial. Some steplike changes in the phase are seen at $\theta=15°$ and 30°. It should be noted that these abrupt phase changes take place just at the frequency positions of the fine structures in the transmission spectra, as seen in comparison with Fig. 4(a). At $\theta=0°$, the clear step in experiment at 50 GHz is not clearly observable because of the large vertical scale of 4π in theoretical calculation.

If the experimental and theoretical phase-shift spectra are compared carefully, one finds that the agreement is apparently not as impressive as the transmission spectra seen in Sec. III A. However, this does not mean that the present theoretical approach involves any significant fault in the phase-shift spectra. To avoid the reference delay of network analyzer, we plot in Fig. 8 the derivatives of the phase-shift spectra with respect to ω for the case of $\theta=15°$. The resolution is not so good in the frequency range above 55 GHz, but the four Lorentzian peaks predicted by the calculation below 55 GHz are clearly observed in the experimental data. In particular, it should be noted that the width and height of the three peaks around $\omega\simeq 50$ GHz are well reproduced by the calculation, as far as the relative magnitudes are concerned.

To summarize the discussion presented in this section, the agreement between the experimental and theoretical results is good for both the magnitude and phase of the transmission EM wave. The remaining part of this paper is devoted to the interpretation of the above results in terms of the monolayer photonic band picture.

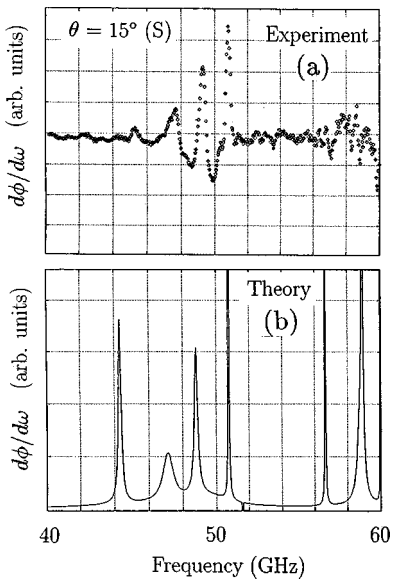

FIG. 8. Phase $\phi(\omega)$ of transmitted S wave differentiated with respect to ω. (a) plots the experimental ω derivative for $\theta=15°$, and (b) shows the theoretical results. The definition of $\phi(\omega)$ is given by Eq. (A12).

IV. THEORETICAL APPROACHES OF FINITE LIFETIME MODES

In this section we propose several methods useful in dealing with photonic bands of the present system. These methods are analyzed in the next section to examine their mutual relationship. The quantities to appear are all defined in previous paper by one of the authors.[27] For the notations not explained fully here, we refer the readers to this reference.

In an array of spherical particles, the incident EM wave suffers a sequential Mie scattering by individual particles. A wave eventually going out of the system has rich information on the photonic bands specified by the 2D wave vector $\boldsymbol{k}$, the lateral component of the wave vector of the incident wave.

Two factors determine the series of the Mie scattering; $\boldsymbol{t}$, the t matrix describing the Mie scattering *within* a single individual scatterer and $\boldsymbol{\Gamma}(\boldsymbol{k})$, the structure factor for the propagation of a photon *among* the scatterers in the lattice. Symbolically, the repetition of the multiple scattering from one sphere to another is represented by the following infinite series:

$$\boldsymbol{t}[1+\boldsymbol{\Gamma}(\boldsymbol{k})\boldsymbol{t}+\boldsymbol{\Gamma}(\boldsymbol{k})\boldsymbol{t}\boldsymbol{\Gamma}(\boldsymbol{k})\boldsymbol{t}+\cdots]=\boldsymbol{t}[1-\boldsymbol{\Gamma}(\boldsymbol{k})\boldsymbol{t}]^{-1}. \tag{4.1}$$

In the actual analysis, $\boldsymbol{t}$ and $\boldsymbol{\Gamma}$ are given their concrete representations in the basis functions of the transverse vector spherical waves. They are specified by the index $L=(l,m)$, which defines the spherical harmonics $Y_{lm}(\theta,\phi)$ in the usual way, and the additional index β, which specifies for each L two vector spherical waves, M and N.[34] These partial waves (β,L) are not mixed in the single-sphere scattering, that is

$$\langle\beta,L|\boldsymbol{t}|\beta',L'\rangle=\delta_{\beta\beta'}\delta_{LL'}t_L^{\beta}, \tag{4.2}$$

with

$$t_L^{\beta}=\frac{-i}{2\omega}\{\exp(2i\delta_l^{\beta})-1\}. \tag{4.3}$$

The last equation defines two phase shifts δ_l^{β} ($\beta=M$ and N). Note that t_L^{β} depends only on l through δ_l^{β}.

The structure factor $\boldsymbol{\Gamma}(\boldsymbol{k})$ causes the mixing between the partial waves in the intersphere scattering. Let $\Gamma_{MN},\Gamma_{NM},\Gamma_{MM}$, and Γ_{NN} describe the mixing with respect to the index β. We introduce a 2×2 block matrix defined by

$$\boldsymbol{t}=\begin{pmatrix}\boldsymbol{t}^M, & \boldsymbol{0}\\ \boldsymbol{0}, & \boldsymbol{t}^N\end{pmatrix},$$

$$\boldsymbol{\Gamma}(\boldsymbol{k})=\begin{pmatrix}\boldsymbol{\Gamma}_{MM}(\boldsymbol{k}), & \boldsymbol{\Gamma}_{MN}(\boldsymbol{k})\\ \boldsymbol{\Gamma}_{NM}(\boldsymbol{k}), & \boldsymbol{\Gamma}_{NN}(\boldsymbol{k})\end{pmatrix}, \tag{4.4}$$

where each block is composed of a matrix labeled by L. The matrices $\boldsymbol{t}^M$ and $\boldsymbol{t}^N$ are diagonal, with the diagonal element t_l^M or t_l^N defined by Eq. (4.3). In terms of $\boldsymbol{t}$ and $\boldsymbol{\Gamma}(\boldsymbol{k})$, the infinite series of Eq. (4.1) is now involved in the inverse matrix $\boldsymbol{B}^{-1}(\boldsymbol{k})$ defined by

$$\boldsymbol{B}^{-1}(\boldsymbol{k})=[\boldsymbol{I}-\boldsymbol{\Gamma}(\boldsymbol{k})\boldsymbol{t}]^{-1}. \tag{4.5}$$

It is important to note that the poles of $\det\boldsymbol{B}^{-1}$ are complex in general due to the finite lifetime effect.

The transmitted and reflected waves from the 2D lattice have the 2D wave vector $\boldsymbol{k}+\boldsymbol{h}$ outside the system, where $\boldsymbol{h}=(h_x,h_y)$ is one of the reciprocal lattice vectors. If $\omega>|\boldsymbol{k}+\boldsymbol{h}|$, channel $\boldsymbol{h}$ is open, that is, channel $\boldsymbol{h}$ has an outgoing plane wave, while, if $\omega<|\boldsymbol{k}+\boldsymbol{h}|$, channel $\boldsymbol{h}$ is closed, having only an evanescent wave characterized by an imaginary z component of $\boldsymbol{k}+\boldsymbol{h}$.

For an incident wave (the $\boldsymbol{0}$ wave) of unit amplitude,

$$\boldsymbol{E}^0(\boldsymbol{r})=\boldsymbol{E}^0\exp[i(\boldsymbol{k}\cdot\boldsymbol{\rho}+\gamma_{\boldsymbol{0}}^{+}z)], \tag{4.6}$$

with $\boldsymbol{\rho}=(x,y),\gamma_{\boldsymbol{0}}^{+}=+(\omega^2-\boldsymbol{k}^2)^{1/2},\boldsymbol{E}_0=(E_x^0,E_y^0,E_z^0)$ and $|\boldsymbol{E}_0|=1$, the transmitted and reflected $\boldsymbol{h}$ waves are then given by $\Sigma_{i'}T_{ii'}(\boldsymbol{h0})E_{i'}^0$ and $\Sigma_{i'}R_{ii'}(\boldsymbol{h0})E_{i'}^0$, respectively, with $i,i'=x,y,z$. Here, $T_{ii'}(\boldsymbol{h0})$ and $R_{ii'}(\boldsymbol{h0})$ are tensor transmission and reflection amplitudes, which take account of the infinite series of Eq. (4.1). For example,

$$T_{ii'}(\boldsymbol{h0})=\delta_{ii'}\delta_{\boldsymbol{h0}}+\frac{\alpha}{\gamma_{\boldsymbol{h}}^{+}}\boldsymbol{Y}^t(\hat{\boldsymbol{k}}_{\boldsymbol{h}}^{+})\boldsymbol{\tau}_{ii'}\boldsymbol{Y}^*(\hat{\boldsymbol{k}}_{\boldsymbol{0}}^{+}). \tag{4.7}$$

The point of this expression is that the quantity $\boldsymbol{\tau}_{ii'}$ is a key quantity related to $\boldsymbol{B}^{-1}(\boldsymbol{k})$. A rather lengthy relationship between them as well as the definitions of other quantities is not reproduced here. The reflection amplitude $R_{ii'}(\boldsymbol{h0})$ is expressed similarly using $\boldsymbol{\tau}_{ii'}$.

Finally, the transmittance $T_{\boldsymbol{h}}$ and reflectance $R_{\boldsymbol{h}}$ associated with channel $\boldsymbol{h}$ are given by the following expressions:

$$|T_{\boldsymbol{h}}|^2=\sum_i\left|\sum_{i'}T_{ii'}(\boldsymbol{h0})E_{i'}^0\right|^2,$$

$$|R_{\boldsymbol{h}}|^2=\sum_i\left|\sum_{i'}R_{ii'}(\boldsymbol{h0})E_{i'}^0\right|^2. \tag{4.8}$$

The diffracted waves, which arise only in extreme cases in our experiments, are not examined in this study; we thus restrict ourselves to $|T_{\boldsymbol{h}=\boldsymbol{0}}|^2$ and $|R_{\boldsymbol{h}=\boldsymbol{0}}|^2$ of Eq. (4.8). They

are denoted hereafter simply as $|T_0|^2$ and $|R_0|^2$,$|T_0|^2$ being just the theoretical expression for the data shown in Figs. 3 and 4. In what follows, we shall describe a number of theoretical approaches to examine photonic bands of finite lifetime.

A. Method using the matrix B (DETB method)

The (pq) matrix element of $\boldsymbol{B}^{-1}(\boldsymbol{k})$ in Eq. (4.5) is given by

$$[\boldsymbol{B}(\boldsymbol{k})^{-1}]_{pq}=\Delta_{qp}/\det \boldsymbol{B}(\boldsymbol{k}), \tag{4.9}$$

using the cofactor Δ_{qp}. From Eqs. (4.7) and (4.8), the transmittance $|T_0|^2$ and the reflectance $|R_0|^2$ must exhibit a resonant divergence when $\det \boldsymbol{B}(\boldsymbol{k})=0$. In other words, the zero points of $\det \boldsymbol{B}(\boldsymbol{k})$ give the eigenfrequencies for the normal modes of the system. These zero-point frequencies are complex in general, as noted above. The quantities $|T_0|^2$ and $|R_0|^2$ would otherwise diverge, when ω is swept along the real axis of the complex frequency plane and crosses the real pole.

The degree of the contribution of each complex pole to the transmitted light is determined by the magnitudes of the matching of Δ_{qp}, in Eqs. (4.7) and (4.8), with the incoming and outgoing waves. Often there is a case where a certain pole of $1/|\det \boldsymbol{B}(\boldsymbol{k})|$ fails to survive in the $|T_0|^2$ or $|R_0|^2$ spectra, indicating that this specific mode is inactive to the incident EM wave. Whether or not a pole is active to an incident EM wave is determined by its group theoretical property (see Ref. 23). If we plot the frequency dependence of a peak of $1/|\det \boldsymbol{B}(\boldsymbol{k})|$ as a function of the wave vector $\boldsymbol{k}=(k_x,k_y)$, we can obtain the theoretical dispersion curves for the corresponding 2D photonic band with a finite lifetime. We refer to this method as the DETB method. By means of this method, one is able to plot the dispersion curves for *all* possible photonic bands, whether optically active or not.

B. Method using increase in DOS

The second method for determining the theoretical dispersion relations is to consider the density of states (DOS) of the complex solutions. The DOS of the eigenphotonic band modes is given by the following expression;[28]

$$N_{\boldsymbol{k}}(\omega)=(1/\pi)(\partial/\partial\omega)\mathrm{Im}\log\det|\,\delta_{\beta\beta'}\delta_{LL'}+\tan\delta_l^{\beta}A_{LL'}^{\beta\beta'}(\boldsymbol{k})|. \tag{4.10}$$

Here, $A_{LL'}^{\beta\beta'}(\boldsymbol{k})$ is the matrix element of a 2×2 block matrix $\mathbf{A}(\boldsymbol{k})$, which is related to the matrix $\mathbf{\Gamma}(\boldsymbol{k})$ by the following relation:

$$\mathbf{A}(\boldsymbol{k})=\mathbf{\Gamma}(\boldsymbol{k})-\mathbf{I}. \tag{4.11}$$

From Eqs. (4.3) and (4.11), we see that the determinant in Eq. (4.10) is essentially that for matrix $\boldsymbol{B}(\boldsymbol{k})$ defined by Eq. (4.5). By plotting the peak positions in the DOS spectra for various values of $\boldsymbol{k}$, the dispersion curves are again obtained. We refer to this method as the DOS method. The width of the DOS peak provides, as usual, information on the magnitude of the lifetime of the corresponding mode.

Here, one comment is in order on the nomenclature of DOS for the quantity defined by Eq. (4.10). Strictly speaking, $N_{\boldsymbol{k}}(\omega)$ is the *increment* of the density of states for photons per single sphere relative to that of the free space. Since we are mainly concerned with the photonic bands originating from the WG modes within the spheres, which is absent in the free space, there is no practical problem in calling $N_{\boldsymbol{k}}(\omega)$ simply DOS.

C. Method using the features in $|T_0|^2$ and $|R_0|^2$ spectra (TR method)

The third method for examining 2D photonic bands is based on the transmittance, which exhibits a number of features whose positions gradually change as θ varies, as shown in Sec. III. These shifts are thought to be related to the dispersion relation of the eigenphotonic band modes. Plotting the *dips* in transmittance $|T_0|^2$, as a function of $\boldsymbol{k}$, we are able to obtain the theoretical band structures. Since the dips in $|T_0|^2$ correspond to the peaks in $|R_0|^2$, we call this method the TR method. The calculated dispersion relations of our 2D monolayer system obtained by the TR method are shown in Figs. 5(b) and 6(b).

D. Optical DOS method (ODOS method)

The last method is based on the use of the phase shift of an incident wave. Detailed analysis is given in the Appendix. For an incident wave of wave vector $\boldsymbol{k}=(k_x,0)$, we may summarize the results as follows.

The optical density of state (ODOS) is obtained by diagonalizing the 2×2 matrix (S matrix) defined by using the transmitted and reflected amplitudes of the incident EM wave. From the unitarity of the S matrix, two eigenvalues of it are expressed in terms of the eigenphase shifts, which we call OPS (optical phase shifts). They are classified according to the polarization and parity [either even $(+)$ or odd $(-)$ with respect to the mirror reflection in the xy layer] of the eigenvectors of the S matrix. For a wave vector $\boldsymbol{k}=(k_x,0)$ of the incident EM wave, directed along the high-symmetry axis of 2D Brillouin zone, we have four OPS, $\delta_{\pm}^{(P)}(k_x,\omega)$ and $\delta_{\pm}^{(S)}(k_x,\omega)$, since the lack of polarization mixing enables us to define and diagonalize the S matrix for each of the P and S cases. The ODOS of the modes belonging to each symmetry is then expressed by

$$N_{k_x,\pm}^{(P)}(\omega)=\frac{1}{\pi}\frac{\partial}{\partial\omega}\delta_{\pm}^{(P)}(k_x,\omega),$$

$$N_{k_x,\pm}^{(S)}(\omega)=\frac{1}{\pi}\frac{\partial}{\partial\omega}\delta_{\pm}^{(S)}(k_x,\omega), \tag{4.12}$$

$N_{k_x,+}^{(P)}(\omega)$, for example, being the DOS of the $+$ parity photonic bands, which are active to a P-polarized incident EM wave. The total ODOS of the 2D photonic bands is given by the sum of these four ODOS.

If we calculate OPS for a fixed value of k_x and plot the peak positions of $N_{k_x,+}^{(P)}(\omega)$, as a function ω, we can trace the dispersion curves for the 2D photonic bands, of $+$ parity and active to the P wave, along the Γ-X axis of the Brillouin zone. The widths of the ODOS peaks again provide informa-

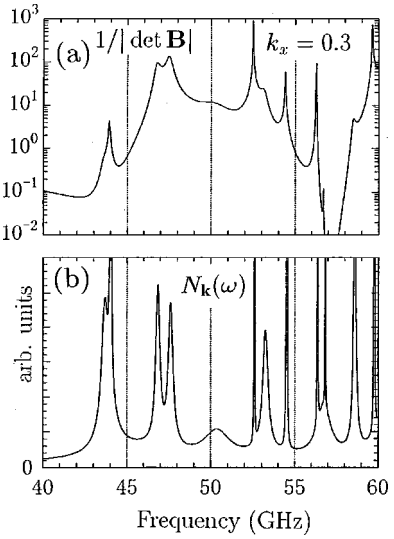

FIG. 9. Theoretical frequency dependences of $1/|\det \mathbf{B}|$ (a) and photonic DOS (b) for the square lattice of Si_3N_4 spheres. The parameters correspond to the spheres used in the present experiment. The horizontal axis is $\omega/2\pi$, and DOS is shown in arbitrary units. The 2D wave vector is fixed at $\mathbf{k}=(0.3,0)$.

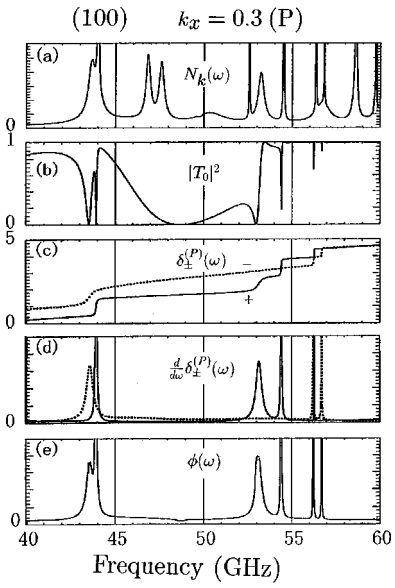

FIG. 10. Frequency dependence of various quantities for P wave. In (a), the DOS shown in (b) of Fig. 9 is reproduced for comparison, which covers all possible photonic modes of $\mathbf{k}=(0.3,0)$. (b), (c), and (d) show, respectively, the frequency dependence of $|T_0|^2 (0 \leq |T_0|^2 \leq 1)$, $\delta_{\pm}^{(P)}$ (in units π) and $(d/d\omega)\delta_{\pm}^{(P)}$ for P wave with the wave vector fixed at $\mathbf{k}=(0.3,0)$. (a) and (d) are given in arbitrary units. In (c) and (d), the results for $\delta_{+}^{(P)}$ are shown by a solid curve and those of $\delta_{-}^{(P)}$ by a dashed curve (in units π). The last figure (e) shows the ω derivative of the phase ϕ of the transmitted amplitude, defined by Eq. (A12). The sum of the results in (d) coincides with (e), verifying the relation given by Eq. (4.13).

tion on their lifetime. We call this method the ODOS method. Note that the ODOS method can cover only those modes that can be excited optically, because OPS are defined using the scattering data of incident EM waves. The point of this method lies in the fact that the combination of the transmitted and reflected amplitudes allows us to separate two modes of different parities. In this respect, it is interesting to note that the phase ϕ of the transmitted amplitude has a relationship with OPS expressed by (see the Appendix)

$$\phi = \delta_{+}^{(P)}(k_x,\omega) + \delta_{-}^{(P)}(k_x,\omega) \tag{4.13}$$

for the phase of the transmitted P wave (the superscript should be changed in the case of S). Namely, the phase of the transmitted amplitude has by itself the information on the sum and fails to distinguish the contributions of different parities. This feature reflects the fact that once an EM wave comes in, the system no longer has mirror symmetry in the plane $z=0$. Therefore, the method used above to recover mirror symmetry in introducing $+$ and $-$ OPS is by no means trivial.

V. FREQUENCY DEPENDENCE OF VARIOUS QUANTITIES

The calculated frequency dependence of $1/|\det \boldsymbol{B}|$ in the DETB method and that of $N_{\boldsymbol{k}}(\omega)$ in the DOS method are plotted in Figs. 9(a) and 9(b), respectively. To obtain them, we have chosen the value $\boldsymbol{k}=(0.3,0)$ for the wave vector $\boldsymbol{k}$ normalized by $2\pi/a_L$. In these units, the X point of the first Brillouin zone is located at $\boldsymbol{k}=(0.5,0)$. In both the DETB and DOS methods, the 2D band structure along the Γ-X axis is obtained by plotting the peak positions as a function of k_x. The corresponding ω-θ relations, as measured in Sec. III, are obtained by using Eq. (3.1). Since the latter are not very different, we present only the band structures versus k_x.

A number of sharp fine structures in Fig. 9(a) are related to the eigenmode frequencies with a nonzero imaginary part. The fine structures are more densely populated and sharper in the higher-frequency region, in agreement with the observation reported in Sec. III. Note that in Fig. 9(a), the width of each peak is different. For example, the small peak at $\omega \simeq 58.5$ GHz is not as sharp as the peaks around 55 GHz. This means that the lifetimes of 2D photonic bands depend on the band index. Also, the peak at $\omega \simeq 44$ GHz is asymmetric, probably due to the overlapping of two Lorentzian peaks. The doublet structure that appears at $\omega \simeq 47$ GHz would merge into a single peak at a value of k_x that is slightly different from 0.3. This corresponds to a band crossing. Because of the damping effect, it becomes harder near the band crossing for the DETB method to distinguish between the behaviors of the two composite bands.

In contrast, the resolution of the DOS method is much higher, as shown in Fig. 9(b). The structures at 44 GHz and 58.5 GHz discussed above are clearly resolved by this method. Also, the doublet structure at 47 GHz in Fig. 9(a) appears as two distinct peaks in 9(b). It is therefore concluded that the DOS method gives a higher resolution than the DETB method. However, the DETB method still works, in view of its general agreement with the results of the DOS method.

A more extensive comparison of various methods is shown in Figs. 10 and 11 for P and S polarizations, respectively. The DOS spectra shown in Fig. 9(b) are reproduced in Figs. 10(a) and 11(a) for comparison. We plot the ω dependence of $|T_0|^2$ of the TR method in Fig. 10(b), OPS in 10(c), its ω derivative (ODOS) in 10(d), and the ω derivative of the phase ϕ of the transmitted wave in 10(e). When Fig. 10(b) is

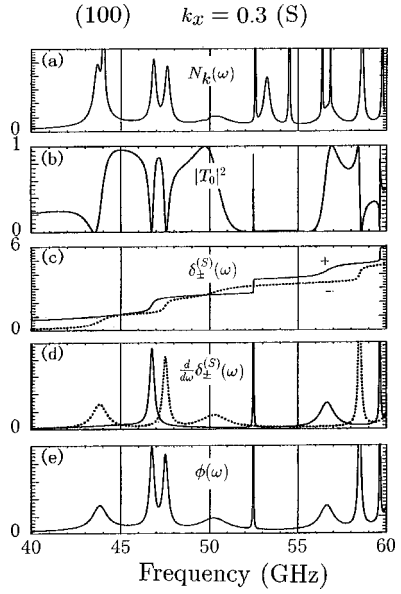

FIG. 11. Plots for various quantities of *S* wave with $\mathbf{k}=(0.3,0)$. The DOS shown in (a) is the same as Fig. 10.(b)–(e) show the results of *S* wave for the same quantities as those in Fig. 10.

compared with 10(a), we find that some peaks in Fig. 10(a) are missing in 10(b). The doublet peak of DOS at 47 GHz is a typical example. From group theory, we know that any 2D photonic band of nonzero $\boldsymbol{k}$ is active on the Γ-X axis either to a *P*- or *S*-polarized wave.[23] Thus, those photonic bands that are missing in the case of *P* should be observable in the case of *S*, as we will see shortly in Fig. 11.

The important point is that the peaks in the DOS spectra [Fig. 10(a)] correspond to the sharp dips in the transmission spectra [Fig. 10(b)]. Therefore, the plotting of dip positions in transmittance in the TR method, as was done to obtain Fig. 5, is concluded to be the right way of obtaining the dispersion relations of photonic bands. (However, for the broad dip observed at 58 GHz of the transmittance, see the discussion below.) Note that the corresponding structures show up as peaks in the reflection spectra, since $|T_0|^2+|R_0|^2=1$ in the frequency range where there is no diffracted wave.

Next, we turn to the spectra shown in Figs. 10(c) and 10(d), 10(c) for the frequency dependences of the two OPS, $\delta_{+}^{(P)}$ and $\delta_{-}^{(P)}$, and 10(d) for their derivatives with respect to ω. There is a stepwise increase in $\delta_{\pm}^{(P)}$ at every dip in transmittance. Note that there is no peak in the ODOS spectra [Fig. 10(d)] at about 48 GHz, where a broad minimum is seen in the transmission spectrum in 10(b). This implies that there is no *P*-active mode in the frequency range from 45–50 GHz, in spite of the apparent existence of a broad dip in the transmission spectrum; therefore, one must be careful to interpret the features in the TR spectra since some of them do not correspond to real photonic bands. Such precaution should also be taken in the plot of dip positions in Fig. 5(a). The experimental points at around 50 GHz appear to split into two branches at $\theta=25°$. However, looking at the spectra at $\theta=30°$ in Figs. 3(a) and 3(b), we find that the lower branch just corresponds to the dip in the $|T_0|^2$ spectrum, which must have been discarded as a false feature in the sense discussed above.

From the peaks in the ODOS spectra shown in Fig. 10(d), it is clear that the overlapping doublet peaks in the DOS spectrum [Fig. 10(a)] at about 44 GHz can be resolved into two definite peaks having different parities. Note that band crossing can only occur between bands of different parities. Thus, we can conclude that the ODOS method allows us to make the most reliable estimation of bandwidths by resolving two overlapping bands of different parities.

The half-width of a photonic band is a measure of its lifetime. The estimated values by the ODOS method are generally of the order of 0.1 GHz. The band showing the broadest half-width (0.5 GHz) of all in the range from 40 to 60 GHz is the one with the lowest frequency. The corresponding Q value is of the order of 10^2.

Figure 10(e) shows the ω derivative of the phase ϕ of the complex transmitted amplitude for *P* incident wave. We find that the peak positions in Fig. 10(e) coincide precisely with those of the DOS spectra given in Fig. 10(a) and those of the ODOS spectra with the results of both parities combined together. The latter fact confirms the relation given by Eq. (4.13).

Figure 11 shows the results for *S* polarization. The topmost plot [Fig. 11(a)] again shows the DOS profile, as in Fig. 10. There are several important points worth noting here. First, the *S*-active ODOS spectra shown in Fig. 11(d) combined with the *P*-active ODOS shown in Fig. 10(d) can duly reproduce all of the whole features of the DOS spectra in Fig. 11(a). For instance, the double DOS peaks located at 47–48 GHz, which were found to be inactive to *P*-polarized wave, manifest themselves as distinct dips in the $|T_0|^2$ spectra of *S* wave, showing that any 2D mode is active either to a *P* or an *S* wave in the oblique case. Second, note that there is a sharp Lorentzian *peak* at 52.5 GHz. This very narrow peak is peculiar in the sense that it shows up not as a dip in transmittance; the observation therefore leads us to conclude that a DOS peak very often gives rise to a dip in transmittance but sometimes induces a peak in transmittance. As for the other three spectra shown in Figs. 11(c)–11(e), discussion similar to the case of *P* is possible.

To summarize, the combined use of information on phase and magnitude of a transmitted wave is important for a full understanding of photonic bands. We can thereby resolve photonic bands of different parities and obtain, accordingly, higher resolution. The band parity is an important factor for determining the crossing or anticrossing effect between two approaching bands.

VI. DISPERSION RELATION OF 2D PHOTONIC BANDS

A. Dispersion relation of damped bands

From the theoretical analysis given in the preceding section, we see that the DETB and DOS methods enable us to plot the dispersion curves of all possible photonic bands, whereas the TR method is able to cover only the modes that are active to a specific polarization of the incident EM wave used. Furthermore, the ODOS method yields the highest resolution and enables us to identify the parity of photonic bands.

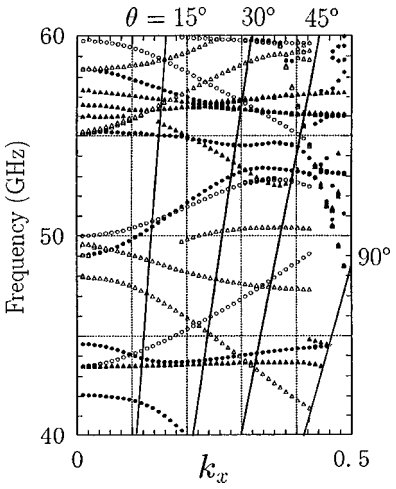

FIG. 12. Band structure of a monolayer square lattice of Si_3N_4 spheres for $\mathbf{k}=(k_x,0)$. The ordinate shows the frequency $\omega/2\pi$ in units of GHz and the abscissa is normalized so that $k_x=0.5$ at the X point of the Brillouin zone. The oblique lines show the ω-k_x relations given by Eq. (3.1) for several values of the incidence angle θ. The bands are classified into four categories according to symmetry (see text for the meaning of the four marks).

The dispersion curves of 2D photonic bands are plotted in Fig. 12 along the Γ-X axis. The results are obtained from the peak positions of the four ODOS, $\partial\delta_{\pm}^{(P)}/\partial\omega$ and $\partial\delta_{\pm}^{(S)}/\partial\omega$. The solid circles (even parity) and solid triangles (odd parity) represent P-active photonic bands, while the open circles and triangles show the even and odd S-active bands, respectively. The ω-k_x relations given by Eq. (3.1) are drawn for several incident angles for comparison with the observations given in Figs. 3(a) and 4(a). Note that only the radiative region in the (k_x,ω) plane, i.e., the left side of the straight line $\omega=k_x$ (the line for $\theta=90°$) is accessible by plane-wave incident light.[35] The points in the upper right corner, where diffraction occurs due to channel opening, are scattered irregularly because the present ODOS method, which neglects the presence of diffracted light, is not correct there.[36]

The experimental points shown in Figs. 3–6 can be well identified with the theoretical plot of Fig. 12, except for the high-frequency region above 55 GHz, where the band population is too dense. Let us relate Fig. 5(a) of P wave with the theoretical bands indicated by the filled marks in Fig. 12. In Fig. 5 (a), there is a branch that goes out of the measured lower-frequency limit when $\theta=20°$. This branch corresponds to the lowest band in Fig. 12. The branch next to it in Fig. 5(a), whose position is almost independent of θ, is caused by excitation of the two flatbands around $\omega/2\pi=44$ GHz in Fig. 12. These two bands approach each other in the range of $k_x=0.2$–0.3, which is consistent with the experiment of Fig. 5(a) or its theoretical fit of Fig. 5(b). The branch observed at 49 GHz at $\theta=0°$ in Fig. 5(a) looks to be a P_+ (an even-parity P-active) branch of Fig. 12. It shifts to a higher-frequency region with the increase of k_x, and at about 53 GHz it crosses a P_- branch that comes from above, leading to overlapping that produces a single dip in $|T_0|^2$ in Fig. 5.

There are several branches in Fig. 12 that cannot be fully traced even by the ODOS method because of the large broadening effect due to a short lifetime. In Fig. 13, a part of Fig. 12 is shown on a magnified scale, where vertical bars are given to illustrate the lifetime-broadened bandwidth; one of the three S_- bands becomes too broad to give the accurate peak position.

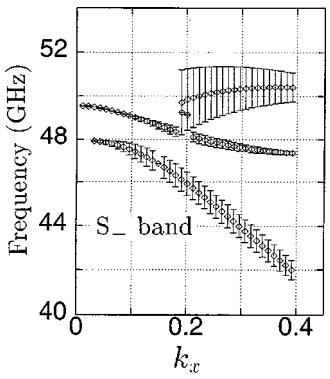

FIG. 13. Examples of very broad bands with the marks of bandwidth attached. The bands that are active to S wave and of odd-parity symmetry are illustrated.

B. Lifetime of Bloch waves

For the estimation of the lifetime of WG modes set up in a dielectric sphere, a well-established method is to differentiate, with respect to ω, the phase shifts $\delta_l^{\mathrm{M}}(\omega)$ and $\delta_l^{\mathrm{N}}(\omega)$ of the single-sphere scattering [see Eq. (4.3)]. The spectra thus obtained takes into account the energy leakage of the (β,L) WG mode, whose decay constant is identified to be the half-width of its peak.

The theoretical spectra for δ_l^{M} and for δ_l^{N} are shown in Figs. 14 and 15, respectively, for a single Si_3N_4 sphere used in the present experiments: (a) for the magnitudes and (b) for the frequency derivatives. The features found in the frequency range from 40 to 60 GHz are attributable to the WG

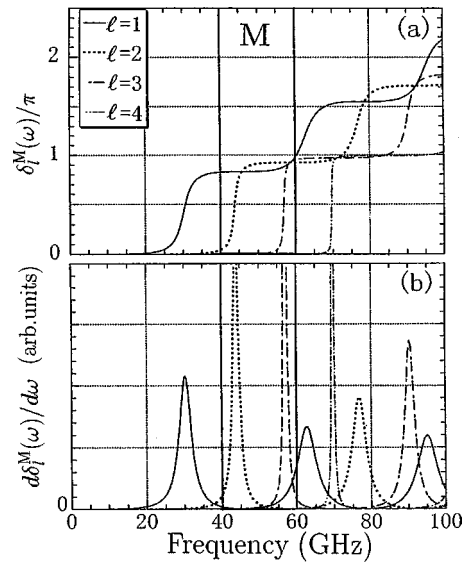

FIG. 14. Calculated phase shifts due to Mie scattering of an Si_3N_4 single sphere. The M phase shifts are given in (a) units π with their ω derivatives in (b) an arbitrary linear scale. The calculation is given for the parameters of $a=3.1/2$ mm and $\varepsilon=8.67$ used in the present experiment. The frequency range of 40 GHz $<\omega/2\pi<60$ GHz is bound by the two bold vertical lines.

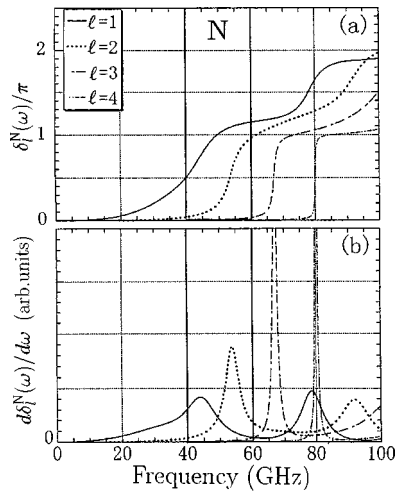

FIG. 15. Phase shifts of *N*-type waves and their ω derivatives for an Si_3N_4 single sphere. See the caption of Fig. 14

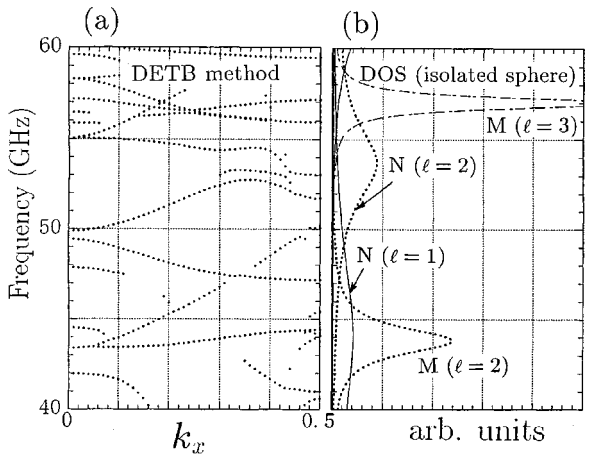

FIG. 16. Band structure of a monolayer square lattice of Si_3N_4 spheres, as compared with the photonic DOS of a single Si_3N_4 sphere. (a) Shows the band structure obtained by plotting the peaks of $1/|\det \mathbf{B}|$. The horizontal axis of (b) shows the ω derivatives of the phase shifts in arbitrary units as functions of $\omega/2\pi$ taken in the ordinate. (b) Reproduces the sum of the *M* and *N* results [Figs. 14(b) and 15(b)], respectively, for the range of 40 GHz$<\omega/2\pi<$60 GHz.

modes of $l=1,2$, and 3. The photonic bands of the 2D lattice we have examined so far are naturally considered to be the superpositions of these lifetime-broadened WG modes, with their $(2l+1)$-fold degeneracy lifted partly. From Figs. 14(b) and 15(b), the radiative half-widths of the WG modes are estimated to be about 5–10 GHz for the $M(l=1,2,3)$ and for the *N* modes $(l=1,2)$, one order of magnitude larger than the widths of the 2D band modes estimated in Sec. V. Thus, our conclusion is that due to the ordering into a 2D periodic lattice, the lifetime of the WG modes generally becomes longer. The reason is that a part of the energy-leakage channels is used in forming the 2D hopping of the WG modes or the 2D dispersion relation of a Bloch wave. However, the lifetime of a 2D Bloch wave is considerably dependent on its band index and wave vector.

To make a more detailed comparison of the band structure with the WG modes of an isolated Si_3N_4 sphere, we reproduced in Fig. 16 the band structure calculated by the DETB method. In contrast to Fig. 12, obtained by the ODOS method, several bands could not be fully traced due to the poorer resolution of the DETB method. In Fig. 16, it is worth noting that the *bandwidths* due to the full dispersion over the first Brillouin zone are nearly of the same order as the FWHM of the WG peaks of a single sphere. Note also that the dispersion is quite large for the bands lying in the frequency range of lower-order modes such as $(N,l=1,2)$ and $(M,l=2)$ of an isolated sphere. In contrast, a group of bands with relatively small dispersion is seen in the higher frequency region, where a sharp WG mode $(M,l=3)$ is located. In this sense, the magnitudes of the energy leakage of the original WG modes are linked with the dispersion curves of the 2D photonic bands.

VII. SUMMARY

The frequency and incidence-angle dependences of transmission spectra were measured in a millimeter wave region on the monolayer of periodically arrayed spheres of Si_3N_4. The observed results were compared with the theoretical calculations. It was found that the observed features in transmission spectra coincide with the theoretical spectra, both in position and breadth. The observed half-widths of the fine structures also show that assembling the spheres into a monolayer lattice generally makes the lifetime longer (roughly ten times) than that in a single sphere. In contrast, the band widths due to spatial dispersion of 2D bands are of the same order of magnitude as the FWHM of the DOS peak of WG modes. These observations suggest that the dominant energy-leakage channel is replaced in a periodic monolayer by the hopping motion between particles and that the radiative decay is greatly suppressed. However, several fine structures observed experimentally showed much broader widths than those obtained by calculation. This minor discrepancy is likely attributable to the nonuniformity in samples due to a slight mismatching in the arrangement. The qualitative analysis of the effect of the small randomness is difficult in our problem and will be an important future problem.

Among the various quantities proposed for theoretical study, the most useful one was found to be the eigenphase shifts derived by combining transmitted and reflected amplitudes. By using them, we could identify each dip (sometimes peak) in transmittance with the excitation of a specific 2D photonic band. The important point of the present analysis is that various theoretical methods used can be straightforwardly applied to a slab photonic crystal of arbitrary thickness. Therefore, the ODOS analysis when applied to a slab photonic crystal will play a crucial role in understanding, say, the lasing in it. Of course, the discussions and conclusions presented in this paper are equally applicable to optical spectra obtained for smaller dielectric spheres such as a latex polymers or SiO_2 particles of diameter in the μm (or sub-μm) range.

APPENDIX

Consider *two* plane-wave lights that are incident on a 2D array of spheres simultaneously from above and below. Their amplitudes are taken to be *a* (from below) and *b* (from

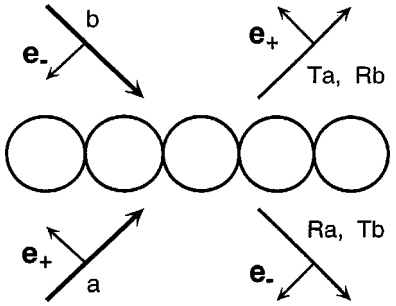

FIG. 17. Two incident waves from $z=\pm\infty$ and their reflected and transmitted components used in introducing the optical phase shifts. The vectors $\mathbf{e}_{\pm}$ are unit vectors specifying the polarization of wave. They are symmetric with respect to mirror reflection in the xy plane. The drawing is given for the P-polarized waves to introduce $\delta_{+}^{(P)}$ and $\delta_{-}^{(P)}$. In the case of S,$\mathbf{e}_{\pm}$ is in the y direction, i.e., normal to the incidence plane.

above). The plane of incidence of waves is assumed to be in the xz plane, as in the text. Let the two waves have the same polarization, either P or S, and 3D wave vectors $(k_x,0,\pm k_z)$. The case for the P polarization is illustrated in Fig. 17. For simplicity, we consider the frequency range where there is no Bragg diffraction. Polarization is conserved in the course of scattering for a lateral wave vector $\boldsymbol{k}$ in the mirror plane as in our case. Let the *scalar* and *complex* coefficients of the transmission and reflection of the waves be T and R, respectively. For the treatment of arbitrary $\boldsymbol{k}$ and ω, where a number of open diffraction channels are allowed to open and the polarization mixing is taken into account, see the comment given in Ref. 36. Far away from the 2D array, the field is then expressed as

$$\boldsymbol{E}(\boldsymbol{r})=\begin{cases}(a\boldsymbol{e}_{+}e^{ik_zz}+(aR+bT)\boldsymbol{e}_{-}e^{-ik_zz})e^{ik_xx} & \text{for } z\simeq-\infty,\\ (b\boldsymbol{e}_{-}e^{-ik_zz}+(bR+aT)\boldsymbol{e}_{+}e^{ik_zz})e^{ik_xx} & \text{for } z\simeq+\infty.\end{cases} \tag{A1}$$

Here, $\boldsymbol{e}_{+}$ and $\boldsymbol{e}_{-}$ are the unit vectors for the polarizations of the upward and downward incident waves, respectively. In the case of P, both $\boldsymbol{e}_{+}$ and $\boldsymbol{e}_{-}$ lie within the xz plane, while in the case of S, they are in the y direction. The second terms in Eq. (A1) represent the scattered waves. Denoting their amplitudes as S_{+} and S_{-}, we have

$$\begin{pmatrix}S_{+}\\ S_{-}\end{pmatrix}=\begin{pmatrix}T & R\\ R & T\end{pmatrix}\begin{pmatrix}a\\ b\end{pmatrix}. \tag{A2}$$

So far, the amplitudes a and b can be arbitrary. From now on, we choose a and b so that the column vector $(a,b)^t$ is an eigenvector of the 2×2 matrix, the S matrix, of Eq. (A2). Then we have

$$\begin{pmatrix}S_{+}\\ S_{-}\end{pmatrix}=\lambda\begin{pmatrix}a\\ b\end{pmatrix} \tag{A3}$$

with an eigenvalue λ of the S matrix, which, from the unitarity of the S matrix, is expressed as

$$\lambda=e^{2i\delta}. \tag{A4}$$

From a given set of T and R of the S matrix, two values are obtained for the eigen phase-shifts. Let us denote them as δ_{+} and δ_{-}, which we call OPS in the text. They depend on the incident polarization through T and R. It follows that

$e^{2i\delta_{+}}=T+R$ for the $[+]$ eigenvector defined as

$$(a,b)_{+}^{t}=\frac{1}{\sqrt{2}}(1,1)^t,$$

$e^{2i\delta_{-}}=T-R$ for the $[-]$ eigenvector defined as

$$(a,b)_{-}^{t}=\frac{1}{\sqrt{2}}(1,-1)^t. \tag{A5}$$

When we put $(a,b)^t$ of Eq. (A1) equal to $(a,b)_{\pm}^{t}$, we obtain two standing waves from Eq. (A1). The $+$ eigenvector yields a standing wave of even parity with respect to the mirror reflection $z\rightarrow-z$, which is expressed as

$$\boldsymbol{E}_{+}(\boldsymbol{r})=\begin{cases}\dfrac{1}{\sqrt{2}}e^{i\delta_{+}}e^{ik_xx}(\boldsymbol{e}_{+}e^{i(k_zz-\delta_{+})}+\boldsymbol{e}_{-}e^{-i(k_zz-\delta_{+})}) & \text{for } z\simeq-\infty,\\ \dfrac{1}{\sqrt{2}}e^{i\delta_{+}}e^{ik_xx}(\boldsymbol{e}_{-}e^{i(k_zz-\delta_{+})}+\boldsymbol{e}_{+}e^{-i(k_zz-\delta_{+})}) & \text{for } z\simeq+\infty.\end{cases} \tag{A6}$$

Since $(\boldsymbol{e}_{+})_x=(\boldsymbol{e}_{-})_x$, $(\boldsymbol{e}_{+})_y=(\boldsymbol{e}_{-})_y$, and $(\boldsymbol{e}_{+})_z=-(\boldsymbol{e}_{-})_z$, its three Cartesian components are written as

$$\boldsymbol{E}_{+}(\boldsymbol{r})=e^{i\delta_{+}}e^{ik_xx}\begin{pmatrix}(\boldsymbol{e}_{+})_x\cos(k_z|z|+\delta_{+})\\ (\boldsymbol{e}_{+})_y\cos(k_z|z|+\delta_{+})\\ i(\boldsymbol{e}_{+})_z(z/|z|)\sin(k_z|z|+\delta_{+})\end{pmatrix}. \tag{A7}$$

In the same way, the amplitude $(a,b)_{-}^{t}$ gives the odd-parity solution $\boldsymbol{E}_{-}(\boldsymbol{r})$, which is expressed as

$$\boldsymbol{E}_{-}(\boldsymbol{r})=e^{i\delta_{-}}e^{ik_xx}\begin{pmatrix}(\boldsymbol{e}_{+})_x(z/|z|)\sin(k_z|z|+\delta_{-})\\ (\boldsymbol{e}_{+})_y(z/|z|)\sin(k_z|z|+\delta_{-})\\ i(\boldsymbol{e}_{+})_z\cos(k_z|z|+\delta_{-})\end{pmatrix}. \tag{A8}$$

The above forms are equally valid for both P- and S-polarized waves: In the case of P polarization, $(\boldsymbol{e}_{+})_y$ is zero, while in the case of S polarization, only the y component remains, because $(\boldsymbol{e}_{+})_x=(\boldsymbol{e}_{+})_z=0$. Thus, the S-polarized standing wave contains only the sine or cosine

function of $|z|$, whereas the *P*-polarized one contains both the sine and cosine functions. This should be so because $\nabla \cdot \boldsymbol{E}_+(\boldsymbol{r})=0$ outside the array. Note that the $\pm$ parity refers to the parity of the lateral components of the standing-wave solutions. Note also that the *P*- and *S*-polarized standing-wave solutions involve different values of $\delta_\pm$. Let us classify them by the symbols $\delta_\pm^{(P)}$ and $\delta_\pm^{(S)}$; there are accordingly four OPS for a given k_x, each giving rise to one standing wave.

Using these asymptotic forms (A7) and (A8), we can determine the normal-mode frequency by confining the field to the region bounded by two perfect mirrors, placed parallel to the xy plane at, say, $z=\pm Z, Z$ denoting a point at infinity. At the mirrors, the field components parallel to the mirror surface must vanish. From Eq. (A7), we then have

$$k_z=\left(n+\frac{1}{2}\right)\pi/Z-\delta_+/Z, \tag{A9}$$

for $n=0,1,2,\ldots$. From Eq. (A8), we obtain for the odd-parity modes,

$$k_z=n\pi/Z-\delta_-/Z. \tag{A10}$$

Then from the well-known procedure of obtaining the increment in DOS,[37] we can obtain the change in the density of states per sphere due to the presence of the array. Using the phase shifts $\delta_\pm^{(P)}(k_x,\omega)$ and $\delta_\pm^{(S)}(k_x,\omega)$, for ω, $\boldsymbol{k}$, and the symmetry $(P,\pm)$ or $(S,\pm)$, the result is

$$N_{k_x,\pm}^{(P)}(\omega)=\frac{1}{\pi}\frac{\partial}{\partial\omega}\delta_\pm^{(P)}(k_x,\omega),$$

$$N_{k_x,\pm}^{(S)}(\omega)=\frac{1}{\pi}\frac{\partial}{\partial\omega}\delta_\pm^{(S)}(k_x,\omega). \tag{A11}$$

This is just Eq. (4.12). The explicit k_x and ω dependences of ODOS are thus expressed by those of OPS.

Next, we relate the phases of T and R with OPS. Since the S matrix of Eq. (A2) is unitary, the quantity TR^* is an imaginary quantity, showing that T and R are of the form

$$T=|T|e^{i\phi},$$

$$R=\pm i|R|e^{i\phi}, \tag{A12}$$

ϕ being a real phase of the transmitted amplitude T. From Eq. (A5), it holds that

$$e^{2i\delta_\pm}=T\pm R, \tag{A13}$$

$$=e^{i(\pm\phi_0+\phi)},$$

with the phase ϕ_0 introduced through

$$|T|\pm i|R|=e^{\pm i\phi_0}, \tag{A14}$$

which holds from the flux conservation $|T|^2+|R|^2=1$. Therefore we find

$$\phi=\delta_+ +\delta_-. \tag{A15}$$

This relation holds for both *P* and *S* polarizations. The conclusion is that the phase ϕ of T of the *P* wave is $\delta_+^{(P)}+\delta_-^{(P)}$ and that of the *S* wave is $\delta_+^{(S)}+\delta_-^{(S)}$; that is, the frequency derivative of ϕ defined by Eq. (A5) gives us the *sum* of $+$ and $-$ODOS. This completes the derivation of Eq. (4.13). The point of making $\pm$ combinations of T and R is that we can thereby single out one of the parities.

[1] E. Yablonovitch, Phys. Rev. Lett. **58**, 2057 (1987).

[2] E. Yablonovitch, J. Phys.: Condens. Matter **5**, 2443 (1993); J. D. Joannopoulos, R. D. Meade, and J. N. Winn, *Photonic Crystals* (Princeton University Press, Princeton, NJ, 1995); *Photonic Band Gaps and Localization*, edited by C,M. Soukaulis (Plenum, New York, 1993); *Photonic Band Gap Materials*, edited by C. M. Soukoulis (Kluwer, Dordrecht, 1996); P. M. Hui and Neil F. Johnson, in *Solid State Physics*, edited by H. Ehrenreich and F. Spaepen (Academic, New York, 1995), Vol. 49, p.151.

[3] J. Opt. Soc. Am. B **10**, (1993), special issue on photonic crystals.

[4] J.D. Joannopoulos, P.R. Villeneuve, and S. Fan, Nature (London) **386**, 143 (1997).

[5] T.F. Krauss, B. Vogel, C.R. Stanley, and R.M. De La Rue, IEEE Photonics Technol. Lett. **9**, 176 (1997).

[6] J.S. Foresi, P.R. Villeneuve, J. Ferrera, E.R. Thoen, G. Steinmeyer, S. Fan, J.D. Joannopoulos, L.C. Kimerling, Henry I. Smith, and E.P. Ippen, Nature (London) **390**, 143 (1997); see also P. Rigby and T.F. Krauss, *ibid.* **390**, 13 (1997).

[7] For the gap modes in photonic crystals, see, for example, K. Sakoda and H. Shiroma, Phys. Rev. B **53**, 7059 (1997), and references therein.

[8] G. Tayab and D. Maystre, J. Opt. Soc. Am. A **14**, 3323 (1997).

[9] S. John, Phys. Rev. Lett. **53**, 2169 (1984). See also, D.S. Wiersma, P. Bartolini, A. Lagendijk, and R. Righini, Nature (London) **390**, 671 (1997), and references therein.

[10] K. Ohtaka and Y. Tanabe, J. Phys. Soc. Jpn. **65**, 2265 (1996).

[11] For the crystallization of polymer spheres, see the articles in *Ordering and Phase Transitions in Charged Colloids*, edited by A.K. Arora and B.V.R. Tata (VCH, New York, 1996); see also P.N. Pusey, in *Freezing and Glass Transition*, edited by D. Levesque, J.-P. Hansen, and J. Zinn-Justin (Elsevier, Amsterdam, 1991) p. 763.

[12] For the recent development of colloidal crystals or artificial opals, see, for example, Judith E.G.J. Wijnhoven and Willem L. Vos, Science **281**, 802 (1998), and references therein.

[13] Xindong Wang, X.-G. Zhang, Qingliang Yu, and B.N. Harmon, Phys. Rev. B **47**, 4161 (1993).

[14] K. Ohtaka, H. Miyazaki, and T. Ueta, Mater. Sci. Eng., B **48**, 153 (1997).

[15] N. Stefanou, V. Karathanos, and A. Modinos, J. Phys.: Condens. Matter **4**, 7389 (1992).

[16] Z.Y. Li, J. Wang, and B.Y. Gu, J. Phys. Soc. Jpn. **67**, 3288 (1998).

[17] I.I. Tarhan and G.H. Watson, Phys. Rev. Lett. **76**, 315 (1996).
[18] I.I. Tarhan, M.T. Zinkin, and G.H. Watson, Opt. Lett. **20**, 1571 (1995).
[19] T. Fujimura, K. Edamatsu, T. Itoh, R. Shimada, A. Imada, T. Koda, N. Chiba, H. Muramatsu, and T. Ataka, Opt. Lett. **22**, 489 (1997).
[20] T. Fujimura, T. Itoh, K. Hayashibe, K. Edamatsu, K. Shimoyama, R. Shimada, A. Imada, T. Koda, Y. Segawa, N. Chiba, H. Muramatsu, and T. Ataka, Mater. Sci. Eng., B **48**, 94 (1997).
[21] E.R. Brown and O.B. McMahon, Appl. Phys. Lett. **67**, 2138 (1995).
[22] K. Ohtaka and Y. Tanabe, J. Phys. Soc. Jpn. **65**, 2670 (1996).
[23] K. Ohtaka and Y. Tanabe, J. Phys. Soc. Jpn. **65**, 2276 (1996).
[24] K. Ohtaka, T. Ueta, and Y. Tanabe, J. Phys. Soc. Jpn. **65**, 3068 (1996).
[25] K. Ohtaka, Phys. Rev. B **19**, 5057 (1979).
[26] W. Lamb, D. Wood, and N.W. Ashcroft, Phys. Rev. B **21**, 2248 (1980).
[27] K. Ohtaka, J. Phys. C **13**, 667 (1980).
[28] K. Ohtaka and M. Inoue, Phys. Rev. B **25**, 677 (1982).
[29] M. Inoue and K. Ohtaka, Phys. Rev. B **26**, 3487 (1982).
[30] H. Miyazaki and K. Ohtaka, Phys. Rev. B **58**, 6920 (1998).
[31] For the radiation damping of a microcavity, see, for example, S.M. Barnett and R. Loudon, Phys. Rev. Lett. **77**, 2444 (1996); H. Becker, R.H. Friend, and T.D. Wilkinson, Appl. Phys. Lett. **72**, 1266 (1998); T. Taneichi and T. Kobayashi, J. Phys. Soc. Jpn. **67**, 1594 (1998).
[32] W.M. Robertson, J. Arjavalingam, R.D. Mead, K.D. Brommer, A.M. Rappe, and J.D. Joannopoulos, Phys. Rev. Lett. **68**, 2023 (1992).
[33] A. Kao, K.A. McIntosh, O.B. McMahon, R. Atkins, and S. Verghese, Appl. Phys. Lett. **73**, 145 (1998).
[34] J.A. Stratton, *Electromagnetic Theory* (McGraw-Hill, New York, 1941), p. 397.
[35] K.L. Kliewer and R. Fuchs, Phys. Rev. **144**, 495 (1966); **150**, 573 (1966).
[36] For a general $\boldsymbol{k}$, the *S* and *P* incident EM waves are mixed in the transmission and reflection. The diagonalization to introduce OPS must then be carried out by using the tensor transmission and reflection amplitudes introduced in Eq. (4.8), instead of the 2×2 matrix used in the appendix. When a number of open diffraction channels coexist, the matrix must be further enlarged to include them.
[37] J.M. Ziman, *Theory of Solids* (Cambridge University Press, Cambridge, England, 1971), p. 146.